crystals

MDPI

Article

Spatiotemporal Changes in Atomic and Molecular Architecture of Mineralized Bone under Pathogenic Conditions

Andrey A. Pavlychev [1,*], Xenia O. Brykalova [1], Alexander A. Cherny [2], Anatoliy V. Korneev [3] and Nikolai N. Kornilov [2]

[1] Department of Physics, St. Petersburg State University, 198504 Saint Petersburg, Russia
[2] National Medical Research Center of Traumatology and Orthopaedics, 195427 Saint Petersburg, Russia
[3] Institute of Earth Sciences, St. Petersburg State University, 199034 Saint Petersburg, Russia
* Correspondence: a.pavlychev@spbu.ru

Abstract: Mechanisms responsible for spatiotemporal changes in the atomic-molecular architecture of the human femur in intact and osteoarthritis-affected areas were studied using high-resolution X-ray diffraction and spectroscopic techniques. Comparison of the experimental data demonstrates strong deviations of core electron-binding energies, lattice constants of hydroxyapatite crystal cells, linear sizes of crystallites, and degrees of crystallinity for both intact and osteoarthritic areas. The quantitative values of these characteristics and their standard deviations in each area are measured and presented. A systematic analysis of the site-dependent deviations was carried out within the framework of the 3D superlattice model. It is argued that the main mechanism responsible for the deviations arises primarily as a result of carbonization and catalytic reactions at the mineral-cartilage interface. The impact of the mechanism is enhanced in the vicinities of the area of sclerosed bone, but not inside the area where mechanical loads are maximum. Restoration of the atomic-molecular architecture of mineralized bone in the sclerosis area is revealed. Statistical aspects of the spatiotemporal changes in mineralized bone under pathogenic conditions are discussed.

Keywords: bone tissue; XRD; XPS; osteoarthritis; hydroxyapatite; bioapatite; biomineralization; atomic-molecular architecture; hierarchical matter; Hellmann-Feynman theorem

Citation: Pavlychev, A.A.; Brykalova, X.O.; Cherny, A.A.; Korneev, A.V.; Kornilov, N.N. Spatiotemporal Changes in Atomic and Molecular Architecture of Mineralized Bone under Pathogenic Conditions. *Crystals* **2023**, *13*, 381. https://doi.org/10.3390/cryst13030381

Academic Editor: Abel Moreno

Received: 30 November 2022
Revised: 20 February 2023
Accepted: 20 February 2023
Published: 23 February 2023

1. Introduction

Biomineralization occurs when morphology, growth, composition, chemical bonding, and local electronic and atomic structures of crystalline phase are governed by cellular effects in a specific organism. The mechanisms controlling biomineralization in bone tissues remain weakly understood. Their research should cut across many interdisciplinary problems and go through different disciplines. The convergence of various approaches and mindsets derived from biological, medical, physical, chemical, and engineering sciences is extremely needed [1].

Being a living substance, bone structures monitor, adapt, and accommodate to various external conditions. In particular, these structures track the distribution of mechanical loads in the skeleton. According to J. Wolff [2], the spatial organization of bone structures is determined during the execution of locomotors body functions against the gravity force. Is this paradigm applicable to bone nanostructures? The electron microscopic studies [3–6] demonstrate a correspondence between the directions of collagen fibrils in the mineralized bone and the force lines that refer to the primary load at each point of the skeleton space. The transverse orientation of collagen fibrils is more common in the cortex that experiences compression, whereas their longitudinal orientation predominates in areas that are primarily stretched [3–6]. The oriented organic molecules of the extracellular matrix of the calcified tissue of vertebrates playing an important role in the structuring of the apatite phase [6–11] initiate biologically necessary substitutions and vacancies through

the aqueous medium [11–14] and form the necessary biochemical environment in the mineralization area [6,15–17].

The impact of mechanical loads, organic molecules, and water on the nanostructure of mineralized bone attracts high attention. A lot of effort has been invested to understand the interplay of the hard hydroxyapatite (HAP, $Ca_{10}(PO_4)_6(OH)_2$) with the flexible collagen fibers, which makes bone more elastic and firmer than the crystal and collagen taken separately [6–8,16–19]. The main morphological models [6–10] are successful in achieving a qualitative description of the hierarchical organization of the skeleton starting from its macro to nano level. However, a quantitative description, especially at the nanoscale, faces great difficulties because the relationships between the upper and lower hierarchical levels have not been studied.

Transmission electron microscopy and X-ray diffraction (XRD) widely used to explore bone structures make evident that coplanar and mosaic assemblies of the nanocrystallites of HAP (NHAP) form the mineral matrix of bone [6–8,17]. According to Newman and Newman [10], NHAPs are separated one from the other by hydrated nanolayers of a saturated aqueous solution containing mainly the OH^-, $[PO_4]^{3-}$, and $[CO_3]^{2-}$ anions and Ca^{2+} cations. According to [19], the effective NHAP in bones is a rectangular block with dimensions $\approx 20 \times 7.5 \times 3.5$ nm^3. Such a nanoblock contains about $4{\cdot}10^4$ atoms. The thickness of the hydrated layer is ≈ 2.5 nm. The NHAPs assemblies generally reproduce the helix shape of collagen fibrils [6].

To bridge the local electronic and atomic structures of the bone with its higher-lying hierarchical levels, the 3D superlattice (3DSL) of "black-nanoboxes-in-muddy-waters" model was suggested [19]. This model takes into account both the qualitative structure-functional organization of mineralized bone and the quantum-mechanical peculiarities of electron waves propagation in 3D superlattices assembled from the NHAPs. The 3DSL model predicts a distinct HAP-to-bone redshift of valence bands [19] and provides a useful tool for controlling the impact of upper-lying hierarchical levels on the atomic-molecular architecture of mineralized bone. Regrettably, the successful application of the model requires the quantification of local electronic and atomic structures and their relationships with the specifics of the organism.

Recently, there has been an explosive interest in mineralized bone regeneration [20]. The regeneration is tightly related to the use of both new synthetic biomaterials (see, e.g., [21–24]) and new methods for controlling the organic—inorganic interactions [25] in native bone. The experimental studies [25–29] make evident that the atomic-molecular architecture of native bone cannot be considered as a fixed structure. The short-, long- and super-range order parameters of NHAPs assemblies are subjects of complicated site- [25,26] and age-dependent [27–29] deviations. These parameters are "fingerprints" of the biological state of mineralized bone and can be used to monitor its development under biogenic or pathogenic conditions.

Specifically, the analysis of concurrent age-related changes in electrons binding energies, degrees of crystallinity, sizes of crystallites, Ca^{2+} deficiency, and HAP lattice constants in bone has shown that the age effects are closely related to charge heterogeneity in the mineral matrix [27]. Thus, mineralized bone is a kind of electric battery composed from nanometric cells formed from negatively charged NHAPs embedded into positively charged intercrystallite water. In contrast, strong site-dependent deviations of structural and spectroscopic parameters are detected in the femur in osteoarthritis (OA) damaged knee compartments [25,26]. According to [25], the site-dependence is motivated by the coupling of mineral and organic matrices. Under normal stress conditions, the sacrificial bonds [30] block the destruction of collagen fibers [30,31]. However, in cases of abnormal stress, when fibers break, their fragments start to interact with NHAPs, producing new non-apatite chemical states. Moreover, the observation of the restoration of calcium bonds and crystallinity in OA-damaged areas [25] provides a new look at the interplay between biochemical and biomechanical processes accompanying biomineralization under

pathogenic conditions. However, the revealed site-dependencies cannot be regarded as quantitative patterns due to low statistics in [25].

In the present work, mineralized bone is examined to understand the nanomechanisms producing its spatiotemporal changes under pathogenic (OA) conditions. High resolution XRD and X-ray photoelectron spectroscopic (XPS) studies of the human femur in intact and OA-affected areas were carried out. XRD studies make it possible to observe the distortion of the crystal structure depending on the spatial distribution of mechanical loads in the skeleton, whereas XPS studies track changes in the chemical bonds in the bone.

The choice of the bone samples, their preparation, and the experimental techniques are described in Section 2. Site-dependent changes in stoichiometry, crystallites sizes, crystallographic lattice constants, degrees of crystallinity, Ca^{2+} $2p_{3/2,1/2}$ electron-binding energies (BEs) are reported and examined in Section 3. The structural and spectroscopic characteristics of mineralized bone under OA conditions were measured for 10 specimens in the identical experimental conditions. The most substantial deviations are revealed near the epicenter of excessive mechanical loads but not inside it. Statistical analysis of the experimental results generally confirms the non-Wolffian patterns in the atomic-molecular architecture under abnormal stress conditions, which were reported in [25]. To understand their nature, the chronobiological concept (Section 3.4) is applied. The identified deviations are primarily associated with catalytic reactions occurring at the organic—inorganic interface and with NHAP carbonization. The peculiarities of these reactions at the interface are due to the coupling of NHAPs with collagen fragments. Perspectives in the experimental and theoretical research of biomineralization under pathogenic conditions are discussed in Section 3 too.

2. Materials and Methods

2.1. Samples Preparation

The medial and lateral condyles of the femur resected during total knee arthroplasty in patients with medial compartmental knee OA were used as samples to study changes in the local electronic and atomic structure of the subchondral bone. Figure 1 displays a radiograph of the OA-damaged knee joint. The sample of healthy bone is a saw-cut of the condyle of femoral bone, not subjected to excessive loads, with intact cartilage (area *1* in Figure 1). The bone sample of the damaged area is a saw cut of the same femoral bone, subjected to excessive mechanical stress due to the development of OA and deformity in the joint, with full-layer loss of cartilage. The area referring to the sclerotic bone is labeled as *2* in Figure 1. Just outside *2* there is a contact region with erased cartilage marked as *3*. Such a choice of objects makes it possible to analyze the subsequence of spatial changes in the bone under the action of mechanical loads.

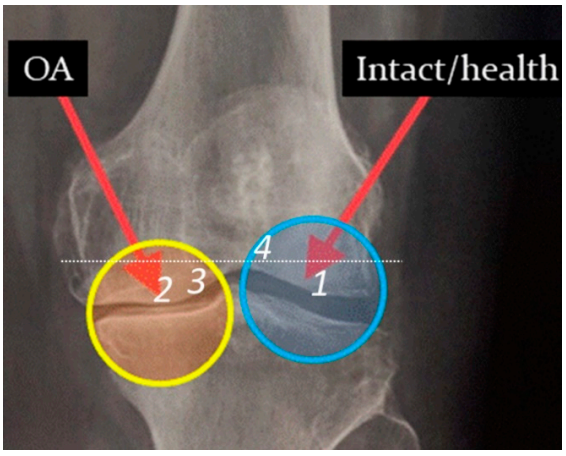

Figure 1. OA-damaged knee joint: different areas on proximal side of the femur: intact *1*, sclerotic bone *2*, and its vicinities *3*. Dots show the position of the distal side (area *4*) of saw-cuts under study.

The bone samples were prepared at the National Medical Research Center of Traumatology and Orthopaedics. The study was approved by the Local Ethical Committee of National Medical Research Center of Traumatology and Orthopedics of the Ministry of Health and Social Development of the Russian Federation. A total of 10 subjects (see, Supplement Materials, Table S1) were examined. All patients have signed an informed consent form.

To prepare the bone samples for the XRD and XPS measurements, in the beginning, the bone saw-cuts were cleaned of cartilage tissue using a gentle mechanical treatment with a scalpel, to subchondral bone plate. Then, to degrease the cuts and remote the myeloid contents from the trabeculae of the spongy layer, the samples were kept for 4 days in a bath with an aqueous 33% hydrogen peroxide solution (H_2O_2) mixed in a 1:1 ratio with hot water (60 °C) and with the addition of 5 mL of 10% aqueous ammonium hydroxide solution (NH_4OH). This mixture was replaced daily. To complete the cleaning process, the samples were placed for one day in distilled water, changing it every 6 h. For the XPS measurements, the samples were additionally subjected to heating at 180 °C for 2 days in thermostat to depress the water evaporation. Just before the XPS measurements, their argon-ions-cleaning was used.

As reference compounds, we used synthetic HAP and synthetic carbonate- hydroxyapatite (CHAP) $Ca_{10-x}(PO_4)_{6-x}(CO_3)_x(OH)_{2-x}$. HAP with an almost stoichiometric composition (a = 9.416(2) Å, c = 6.880(1) Å) was synthesized by applying the reverse precipitation method in an ammonium-containing solution. This method is described in [32,33]. CHAP with CO_3 concentration (wt = 5%) was synthesized by precipitation method too, which included a solution containing 100 mL of a 0.1 M solution of NH_4 hydrogen phosphate and a solution of NH_4 hydrogen carbonate with a molar ratio of C/P = 0.05. Synthesis of apatite was carried out at a temperature of 85–90 °C and pH = 8–10, which was achieved by adding NH_4 hydroxide to the solution. After completing the precipitation process, the solution was kept at 90–100 °C for 2 h, then the precipitate was filtered off, washed with distilled water, and dried in an oven at 110 °C for a day.

2.2. Experimental Methods

The XRD and XPS measurements of the samples were performed for the intact and OA-damaged areas on the proximal and distal sides of the saw cuts. The XRD measurements were carried out by using the high-resolution diffractometer D8 Discover (Bruker, Germany). The XPS measurements were carried out by using the photoelectron spectrometer Thermo Fisher Scientific Escalab 250Xi. No samples charging or decomposition effects were detected during the studies. The measurements were recorded several times and have demonstrated good reproducibility. To extract the structural parameters such as crystal phase composition, degrees of crystallinity, average linear sizes of crystallites, and lattice constants, the Rietveld refinement (see, e.g., [34]) was applied to the XRD data. XPS is a well-known method providing sensitive probing of chemical bonds in surface layers [35,36]. In our case, their thickness is estimated at ≈10 nm.

Voigt functions-were used to fit the experimental Ca $2p_{3/2,1/2}{}^{-1}$ PE lines corresponding to single-hole ionization from the specimens in different areas. This analysis (see, e.g., [25–27]) makes it possible to document the Ca $2p_{3/2,1/2}$ electron BEs and extract the Lorentzian and Gaussian widths of the PE lines. These widths can be assigned with the Ca^{2+} 2p-hole life time as well as with the bandwidth of photon source and inhomogeneous imperfectness of NHAPs, respectively. The single-Voigt-function approximation reproduces precisely the PE lines in HAP, CHAP, and areas *1* and *4*, but not in areas *2* and *3*. In the latter case, the number of Voigt functions increased, so that one of them coincided with the function that reproduces the signal from the intact area.

3. Results and Discussions

To illustrate the site- and patient-dependences of X-ray diffraction and photoemission measurements, sets of XRD patterns and Ca $2p_{3/2,1/2}{}^{-1}$ PE spectra of the specimens are

shown in Figures 2 and 3, respectively. These experimental data were used to extract structural and spectroscopic parameters of the atomic-molecular architecture in the different areas. The extracted site-dependent changes of crystallinity, lattice constants *a* and *c*, and population of apatite Ca^{2+} states are presented in Figure 4a–c. In the plots to display the spatiotemporal changes, a chronobiological order *1*→*3*→*2* is used. It refers to the transitions from healthy bone with a full-layer cartilage (area *1*) to its partially damage (area *2*) and, then, to its full loss (area *2*). This arrangement is discussed in more detail in Section 3.4.

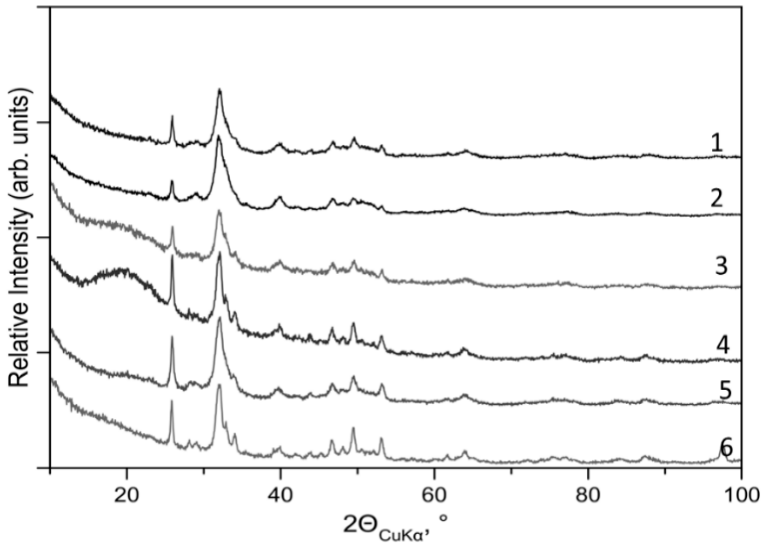

Figure 2. As an illustration, XRD patterns of mineralized bone found in different areas and specimens (see, Supplement Materials, Table S1). 1—(area *4*; sample *i*), 2—(*3*; *viii*), 3—(*3*; *iii*), 4—(*2*; *iii*), 5—(*1*; *i*), 6—(*1*; *iii*).

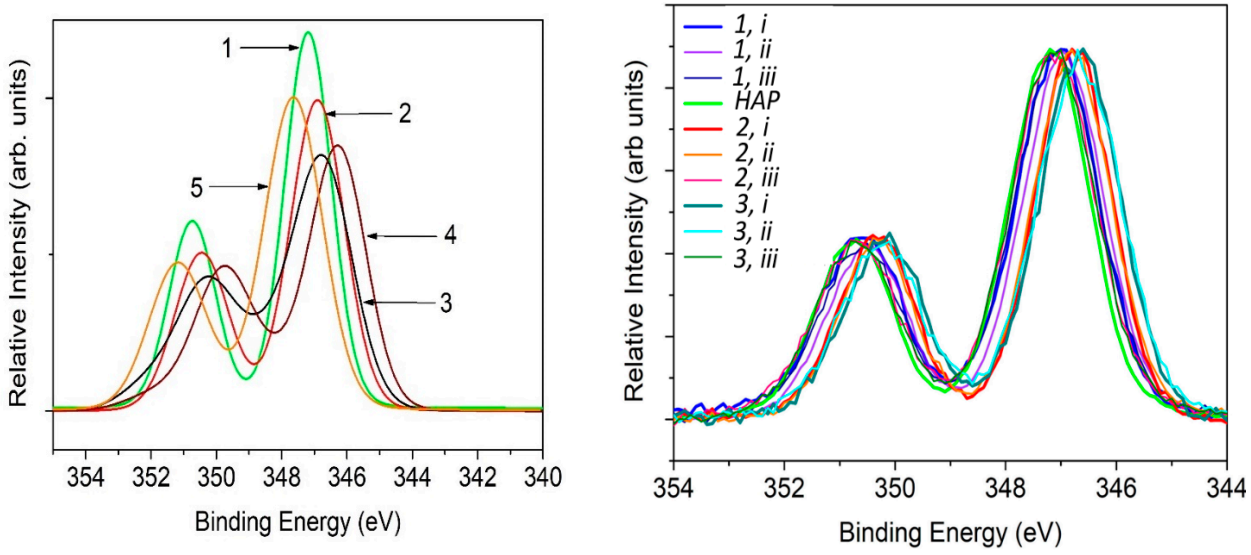

Figure 3. (**a**) General view of the spectral changes in the shape of the Ca^{2+} $2p_{3/2}{}^{-1}$ ad $2p_{1/2}{}^{-1}$ PE lines: HAP (curve 1), CHAP (curve 5), healthy bone (red, curve 2), sclerotic bone (black, curve 3), and vicinities of the sclerotic bone (dark red, curve 4). (**b**) Site- and patient-dependences of Ca $2p_{3/2}{}^{-1}$ and $2p_{1/2}{}^{-1}$ PE lines in bone. *1*, 2, *3* and *i*, *ii*, *iii* indicate the area number and sample number, respectively, (see Supplementary Material, Table S1). The reference Ca^{2+} $2p_{3/2'1/2}{}^{-1}$ PE spectrum of HAP (green) is also shown.

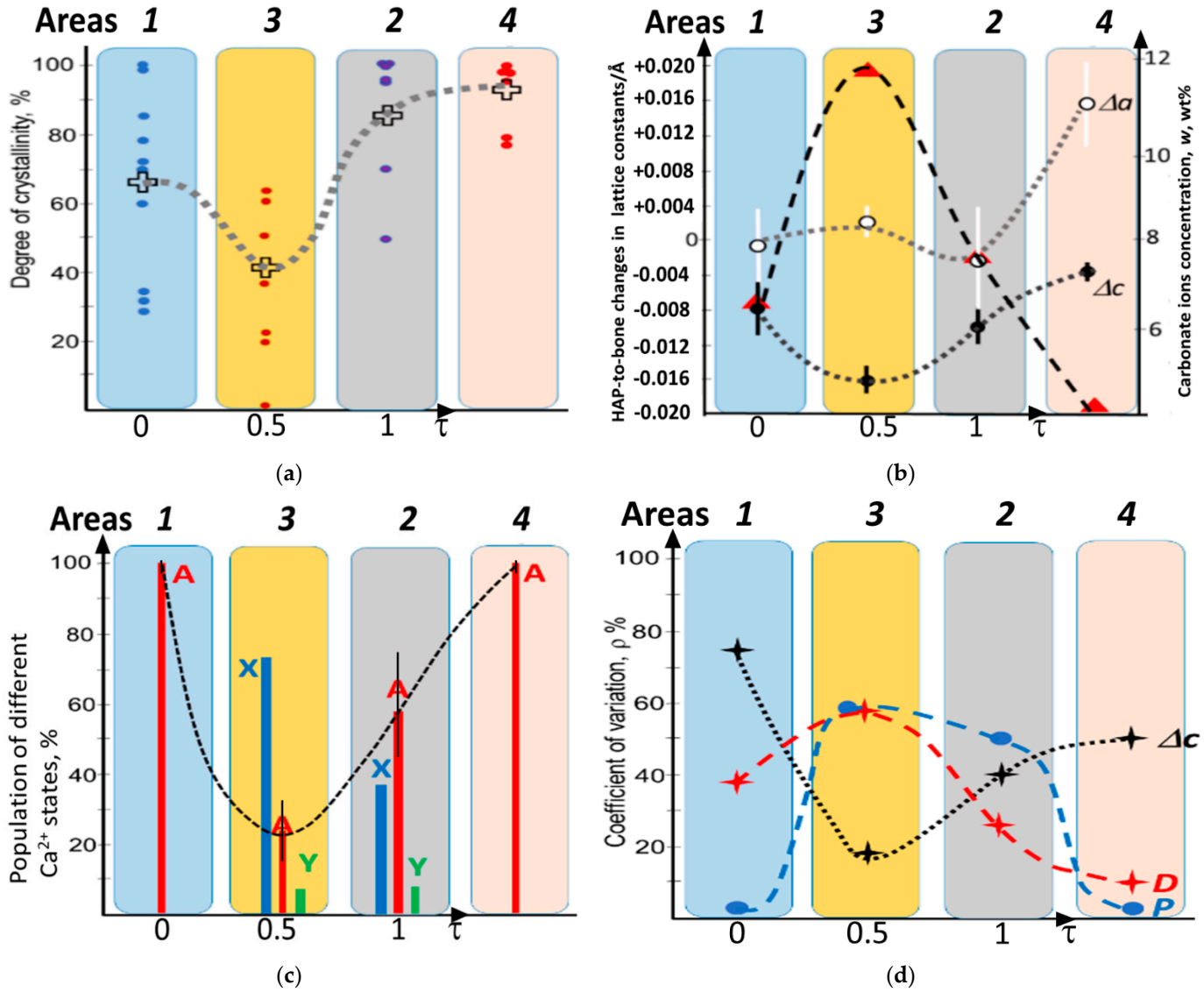

Figure 4. Site−dependent changes of structural and spectroscopic characteristics in the specimens. Colored rectangles correspond respectively to areas *1*, *2*, *3*, and *4*. (**a**) Degrees of crystallinity. *D* values corresponding to different specimens are shown with dots; crosses mark the average degree for each area; and dotted line demonstrates the site-dependent variations of average crystallinity. (**b**) HAP-to-bone changes in the lattice constants (left scale): black dotted line (Δc), grey dotted line (Δa); and white and black vertical bars indicate the standard deviations for *a* and *c*, respectively. Dash line presents the site-dependence of the carbonate ions concentration *w* (right scale); (**c**) mean population of various chemical states of Ca^{2+}: Ca^{2+}(A) red; Ca^{2+}(X) blue; and Ca^{2+}(Y) green; and vertical bars indicate the standard deviations for P_A (**d**) Coefficient of variation. ρ_D (red cross), ρ_P (blue dot), and $\rho_{\Delta c}$ (black cross). The horizontal axis also shows changes in the temporal parameter τ that describes changes under OA conditions: $\tau = 0$ (healthy bone), $\tau = 0.5$ (erased cartilage), and $\tau = 1$ (sclerotic bone).

3.1. XRD Data Analyses

No other crystal phases excepting hexagonal HAP (space group $P6_3/m$) are revealed in the bone samples. The XRD data analyses make evident the distinct site- and patient-dependent deviations of degree *D* of crystallinity, linear size *L* of NHAPs, and crystallographic lattice constants *a* and *c*. The site-dependent changes in *D*, *a* and *c*, are respectively displayed in Figure 4a,b.

3.1.1. Crystallinity

Examining Figure 4a, we observe a noticeable spread of the degrees of crystallinity, which specifies both the site- and patient-dependent variations. The average degree $\langle D \rangle$ for each area is marked with a cross. The dotted line traces its site-dependent behavior. As it was mentioned, above the degrees are arranged in the figure in chronobiological order *1*→*3*→*2*. To get a more complete picture, the degrees of crystallinity detected far from the frontal areas on the distal side (*4*) are also shown.

On the distal side, the degree $\langle D \rangle$ is maximum (90%) and does not practically vary when moving along it. An opposite situation is realized on the proximal side, in which the degrees vary significantly. The lowest $\langle D \rangle$ (≈42%) is observed in the vicinities of the sclerotic bone (area *3*). $\langle D \rangle$ is equal to 65% in *1* and to 85% in *2*. These variations agree reasonably with those reported in [25]. Moving in the direction from *1* to *3* and, then, to *2*, we first fall into the region of hard destructions, and then relocate to the region, where the degree of crystallinity increases, pointing to the remineralization (restoration) of the apatite phase. Despite the general resemblance of the site-dependent changes to those reported in [25], there are substantial difference as the $\langle D \rangle$ does not display such strong destruction (amorphization) in *3*. The measured standard deviations of crystallinity σ_D are equal ≈23% in areas *1*–*3* and ≈9% in *4*.

3.1.2. Lattice Constants

The site-dependence of the lattice constants a and c and their HAP-to-bone differences (Δa and Δc) are plotted in Figure 4b. The differences are defined as

$$\Delta a(c) \equiv a(c)_{\mathrm{HAP}} - \langle a \rangle (\langle c \rangle)_{\mathrm{bone}}, \quad (1)$$

where $\langle a \rangle$ and $\langle c \rangle$ are the averaged values of the constants. The lattice constants, HAP-to-bone differences, and standard deviations in the areas are illustrated in Table 1. Examining these data, the c-stretching ($\Delta c < 0$) in bone is clearly visible for all areas. We hypothesize that c-stretching is a general phenomenon in bone under OA conditions. This stretch is a distinct effect as the standard deviation $\sigma_c < |\Delta c|$. Another behavior is detected for the lattice constant a. It is substantially compressed on the distal side ($\Delta a > 0$) and close to the stoichiometric HAP value on the proximal side, where the standard deviation σ_a is greater than $|\Delta a|$. The volume V of HAP crystal cells in bone is enlarged on the proximal side but stressed on the distal side. Volume versus location variations associated with the stoichiometric HAP (R_{vol}) is shown in Table 1 (last column).

Table 1. Site dependence of lattice constants $\langle a \rangle$ and $\langle c \rangle$ in bone, HAP-to-bone changes Δa and Δc, standard deviations σ_a and σ_c; ratio ($R_{vol} = V(\mathrm{bone})/V(\mathrm{HAP})$) of crystal cell volumes in bone to that in stoichiometric HAP. Lattice constants, HAP-to-bone changes, and standard deviations are given in Å.

Areas	Δa	$\langle a \rangle$	σ_a	Δc	$\langle c \rangle$	σ_c	R_{vol}/a.u.
1	−0.001	9.419	0.009	−0.008	6.892	0.006	1.0014
2	−0.003	9.421	0.012	−0.010	6.894	0.004	1.0021
3	+0.002	9.416	0.003	−0.017	6.901	0.003	1.0020
4 (Distal side)	+0.015	9.403	0011	−0.004	6.888	0.002	0.9974

The variations of the lattice constant c attracted our attention. Comparing them with the variations of crystallinity in Figure 4a, we see their close resemblance. Both the greatest stretch of the constant and the biggest depress of D occur in the intermediate area *3*. Therefore, we can assume that the uniaxial stretching of the crystal cell and the reduction of crystallinity are interrelated events in bone mineral under OA conditions. It is known [37–39] that c-stretching in biogenic HAP is usually motivated by the replacement of $[PO_4]^{3-}$ by $[CO_3]^{2-}$. It is also known that the constant c increases nearly linearly with increasing concentrations (w) of $[CO_3]^{2-}$ [37]. Then, taking into account both the linear $w(c)$

dependence [37] and the average values of c from Table 1, we computed the concentrations of carbonate ions in various areas of the studied specimens. These concentrations are shown in Table 2. Considering them, we see that the concentration of $[CO_3]^{2-}$ on the proximal side is higher than that on the distal one, and the maximum of carbonization is at *3*. The extracted site-dependency w is shown with the dashed line in Figure 4b.

Table 2. Concentration of $[CO_3]^{2-}$ in mineralized bone in different areas of femur in OA-damaged compartment.

Concentration of $[CO_3]^{2-}$\Areas	**1**	**2**	**3**	**4**
w wt%	6.55	7.65	11.6 *	4.15

* The limiting concentration of $[CO_3]^{2-}$, taking into account water molecules, is 14.2% [15].

3.1.3. Sizes of Crystallites

The site dependence of the linear size of NHAPs is not discussed here. We note that the average size $\langle L \rangle$ is ≈20 nm on the distal side, ≈15 nm and ≈11 nm on the proximal side in the intact and sclerotic areas, respectively. In *3*, the size variations are very significant. Obviously, more statistics are needed to study the dependence. Tentatively, this uncertainty can be assigned to the low crystallinity in *3*.

3.2. XPS Data Analyses

The Ca^{2+} $2p_{3/2,1/2}{}^{-1}$ PE spectra of the HAP and CHAP reference compounds and native bone samples are exhibited in Figure 3. The distinct energy shifts and line shapes distortions are clearly visible. We draw attention to the downward shift of the Ca^{2+} $2p_{3/2,1/2}{}^{-1}$ PE lines in the bone specimens compared to those in the reference minerals. To document the energy shifts and the line shape distortions, the measured spectra were examined using the Voigt fit analysis.

According to this analysis, the Ca $2p^{-1}{}_{3/2}$ and $2p^{-1}{}_{1/2}$ PE lines shapes corresponding to HAP and CHAP, as well as to intact areas on the proximal side and over all areas on the distal side are precisely reproduced with the single-Voigt-function approximation. The Ca $2p_{3/2}$ and $2p_{1/2}$ spin-orbit components are split ~3.55 eV; the Gaussian width completely dominates in the full-width-at-half-maximum of the individual Ca^{2+} $2p_{3/2}{}^{-1}$ and $2p_{1/2}{}^{-1}$ components, and their relative intensity is close to 2:1. The simple composition of the spin-orbit split components allows us to assign them to the PE emission from the Ca^{2+} apatite states. In bone tissues, they are denoted via Ca^{2+}(A), the corresponding Ca^{2+} $2p_{3/2}$ BE is disposed in the range 347.1–347.0 eV. Thus, the apatite-like calcium dominates (its population P_A is nearly 100%) in the intact area and on the distal side of the saw-cuts. Another situation is realized in OA-damaged areas, where the single-Voigt-function approximation does not work. At least three components must be included to reproduce the PE signals from the areas. In addition to Ca^{2+}(A), the measured Ca^{2+} $2p_{3/2,1/2}$ PE lines contain the PE fluxes outgoing from non-apatite calcium states denoted as Ca^{2+}(X) and Ca^{2+}(Y). The Ca^{2+}(X) $2p_{3/2}$ BE is disposed at ≈346.5 eV, and the Ca^{2+}(Y) $2p_{3/2}$ BE is disposed at 348.2–348.0 eV.

Figure 4c demonstrates the decompositions of the Ca^{2+} $2p_{3/2}$ photoelectron signals emitted from the different areas in the specimens. It can be seen that areas *1* and *4* are predominantly populated by Ca^{2+}(A), whereas its population decreases in areas *2* and *3*. The average population P_A is 57.5% in *2* and 22% in *3*. Our measurements show that Ca^{2+}(X) plays an important role in the areas since its population P_X is 36,5% in *2* and 73% in *3*. As for Ca^{2+}(Y), its part is nearly 5–6%. In more than half of the bone samples, Ca^{2+}(Y) was not practically visible. The average site-dependent population of Ca^{2+}(A) is shown with a dashed line in Figure 4c. The standard deviations of P_A are less than 5% in areas 1 and 4, ≈29% in *2* and ≈18% in *3*.

The accurate assignment of the non-apatite calcium bonds in the OA areas is a difficult problem. Note that the $Ca^{2+}2p_{3/2}$ BEs in HAP, α- and β-tricalcium phosphates (TCP), amorphous calcium phosphate (ACP), octacalcium phosphate, and brushite vary in a narrow range of 347.0–347.3 eV [40,41]. These BEs are presented in Table 3. The calcium—phosphate bonds are not considered as a main source of non-apatite Ca^{2+}(X) and Ca^{2+}(Y) states, the Bes of which are located far from the indicated range. In $CaCO_3$ polymorphs, the relevant BEs vary in a wider range. According to [40], the $Ca^{2+}2p_{3/2}$ BE is 346.5 eV in calcite and 347.9 eV in aragonite. Thus, the Ca^{2+}(X) can be tentatively assigned with calcium ions with calcite-like bonds [25]. Since in mineralized bone there are no crystal phases except for HAP, amorphous calcium carbonate is a plausible candidate for the role of Ca^{2+}(X). Regrettably, its effect in bone is less studied than ACP (see, [42–44]).

Table 3. Ca^{2+} $2p^{-1}{}_{3/2}$ BEs in bone and calcium phosphates and carbonates.

Objects	BE/eV	Objects	BE/eV
HAP	347.2 [1]; 347.13 [2]; 347.2 [3]	Brushite	347.3 [1]
CHAP	347.64 [3]	α-TCP	347.2 [1]
cortex, young rats	346.9 [4]	β-TCP	347.0 [1]
cortex, mature rats	347.1 [4]	calcite ($CaCO_3$)	346.5 [5]
human femur (intact)	347.0 [3]	aragonite ($CaCO_3$)	347.9 [5]
ACP	347.1 [1]		

[1] Data from Ref. [40], [2] Data from Ref. [41]; [3] this work, [4] Data from Ref. [27]; [5] Data from Ref. [45].

The comparison of Ca^{2+} $2p^{-1}{}_{3/2}$ BEs in calcium phosphates and carbonates in Table 3 shows that the carbonization gives rise to the Ca^{2+} $2p^{-1}{}_{3/2}$ Bes compared to HAP. The energy positions of the Ca^{2+} $2p^{-1}{}_{3/2,1/2}$ PE lines in CHAP (curve 5 inFigure 3a) are lower than those in HAP (curve 1). Thus, we infer that the replacement of $[PO_4]^{3-}$ by $[CO_3]^{2-}$ is not a source of Ca^{2+}(X) in XPS, as accounting for this carbonization does not compensate the contribution of Ca^{2+}(X) to the PE lines composition in Figure 4c.

The similarity of the site-dependent variations in P_A, D, and lattice constant c indicates the important role of chemical reactions occurring at the interface between damaged cartilage and NHAPS, as well as their close relationship with the Wolff's biomechanics in the formation and orientation of bone nanostructures in subchondral bone under pathogenic conditions.

3.3. Coefficients of Variation

The coefficient of variations ρ_j for crystallinity, populations of Ca^{2+}(A), and stretching of the lattice constant c was examined too. The coefficient defined as $\frac{\sigma_j}{\langle j \rangle}$ (where the numerator is a standard deviation of j and denominator is the averaged value of j) shows the degree of variability in relation to the sample mean. Figure 4d presents the site-dependence of the coefficients for D, Δc, and P_A. It is seen that they vary non-monotonously and come through extremums at *3*. In contrast to $\boldsymbol{\rho}_D$ and $\boldsymbol{\rho}_P$, which demonstrate maximal variability in this area, the coefficient $\boldsymbol{\rho}_{\Delta c}$ points to the minimal variability of Δc in it. This specificity confirms our assignment of the c-stretching with the concentration of $[CO_3]^{2-}$ in NHAPs. Since the concentration in the vicinities of the sclerosis areas approaches the saturation limit (see, Table 2), the depress of $\boldsymbol{\rho}_{\Delta c}$ in *3* is expected. As for $\boldsymbol{\rho}_{\Delta a}$ not plotted in the figure, the differences Δa demonstrate an extremely high variability. The only exception is the distal side, where $\boldsymbol{\rho}_{\Delta a} \approx 73\%$. We emphasize that the site-dependence of the standard deviations of D, c, and P_A and their mean values differ substantially.

3.4. Chronobiological Concept

The systematic and site-dependent changes in crystallinity, lattice constants, carbonization, and electron BEs of the human femur under pathogenic (OA) conditions are revealed. For all studied samples, the HAP-to-bone changes are maximum when scanning along the

proximal side, vary substantially when moving in depth to the distal side, and demonstrate minor deviations by monitoring the distal side. The most intense reduction in crystallinity, stretching of the HAP lattice constant c, growth of carbonization, and rupture of apatite chemical bonds take place on the proximal side in the vicinities of the sclerotic bone (area *3*). Specifically, inside the sclerosis area where the mechanical loads are maximum, the values of c, D, w, and P_A approach those in healthy bone (in our case, these are the values in areas *1* and *4*). This site-dependence is quite unexpected from the standpoint of Wolff's paradigm, according to which the strongest deviations should be expected in the sclerosis areas but not in their vicinities. This finding shows that the nature of the spatial changes in mineralized bone under OA conditions is primarily related to biochemical reactions occurring at the organic—inorganic interface. It is these reactions at the interface that generate the greatest changes in *3* and produce the non-apatite calcium states in areas *2* and *3*.

These non-apatite states not inherent in healthy bone are a trigger of the complex reconstruction of the atomic-molecular architecture of bone in the setting of OA. For a better understanding of the mechanisms of reconstruction, we consider the site-dependent changes as spatiotemporal. The structural and spectroscopic characteristics in the areas *1*, *2*, and *3* can be associated with different degrees of OA development. Hence, the site-dependencies are closely related to temporal changes in the bone samples, and one can speak of their spatiotemporal changes.

To quantify the temporal changes in native bones, we consider their characteristics on the nanoscale as functions of a continuous parameter, introduced as $\tau \equiv t/T$, where t and T are the time counted from the onset of the disease and time-period up to full loss of cartilage, respectively. Thus, τ is the dimensionless parameter that characterizes the totality of changes in the atomic-molecular architecture of the bone occurred by a given point in time. Thus, the dependencies of D, Δc, Δa, ω, and P_A on τ is a consequence of the hierarchical organization of the mineralized bone and reflects its emergent properties. To specify the temporal changes in these observable characteristics, we turn to the Hellmann–Feynman theorem (see, e.g., [46])

$$\frac{dE(\tau)}{d\tau} = \left\langle \psi(\tau) \left| \frac{dH(\tau)}{d\tau} \right| \psi(\tau) \right\rangle. \quad (2)$$

Here, $H(\tau)$ is a Hamiltonian of the biological system that depends on τ, $\psi(\tau)$ is an eigenfunction of the Hamiltonian, and $E(\tau)$ is the corresponding eigenvalue. The function ψ is determined by the stationary Schrödinger equation. Thus, we can distinguish the parametrical dependence of the characteristics on τ from the time (t) dependence due to $\psi = \psi(\boldsymbol{r}, \boldsymbol{R}; \tau)e^{2\pi i E t/h}$, where $\boldsymbol{r}$ and $\boldsymbol{R}$ are the electronic and nuclear variables in the skeleton frame. Such distinguishing becomes possible as the biological system is in a non-equilibrium state.

Taking into account the parametrical dependence, we consider the spatial changes in the sequence intact area *1* → vicinities of the sclerosis area *2* → sclerosis area *3* in Figure 4a–c as the corresponding temporal changes in $D(\tau)$, $\Delta c(\tau)$, $\Delta a(\tau)$, $\omega(\tau)$, and $P_A(\tau)$ as τ increases from 0 to 1. Looking at the graphs, we see that the most dramatic destruction of the atomic-molecular architecture of mineralized bone occurs upon its contact with the damaged collagen fibers. After their complete removal in area *2*, bone regeneration becomes the prevailing trend. Thus, we can assume that the opposition of catalytic processes caused by OA and cellular effects determines the atomic-molecular architecture in *3*, and the resumption of the biomineralization process controls it in *2*.

4. Conclusions

The distinct site-dependent deviations in crystallinity, HAP lattice constants, carbonization, core-electron Bes, and calcium bonds in mineralized bone under OA conditions were revealed. The quantitative values of these characteristics and their standard deviations in each area were measured. The strongest OA-induced distortions were concentrated

on the proximal side in the vicinities of sclerotic bone, where the erased cartilage come into contact with the mineral matrix. These distortions consist primarily in reduction of crystallinity, stretching of the lattice constant *c*, and dominance of new chemical states that are not characteristic of HAP. This site-dependence of the structural and spectroscopic characteristics of mineralized bone under OA conditions is a general phenomenon that was detected in all samples.

There are two main mechanisms leading to the distortions. The first is associated with (i) the replacement of $[PO_4]^{3-}$ by $[CO_3]^{2-}$, the concentration of which approaches saturation limit in the vicinities of the sclerosis area, and with (ii) the increase in catalytic reactions provoking the breaking of calcium bonds in HAP at the mineral-collagen interface. The second mechanism is related with cellular effects resulting in the restoration of mineralized bone within the sclerosis area as after the loss of cartilage tissue, the characteristics of the atomic-molecular architecture in 2 approach those of healthy bone.

It is stated that the atomic-molecular architecture of the mineralized phase varies under the action of mechanical loads, but also depending on its localization in the bone space. This architecture on the proximal side differs significantly from that on the distal side. In particular, on the distal side we see the substantial increase of crystallinity, sharp shortening of the lattice constant *a*, as well as a strong reduction in the concentration of $[CO_3]^{2-}$ compared to the corresponding values within the intact area on the proximal side.

Finally, we note that fine tuning of the ion exchange processes in native bone aimed at its treatment and restoration is impossible without a thorough study of the mechanisms of biomineralization under both biogenic and pathogenic conditions. Further experimental and theoretical investigations are required to (i) identify the non-apatite calcium bonds in the OA-damaged areas, (ii) establish a relationship between chemical reactions at the interface, changes in crystallinity, and crystal lattice parameters, and (iii) understand their interplay with cellular effects in a specific organism. We believe that further studies of the atomic-molecular architecture of bone tissue will make it possible to understand the relationship between biomineralization and age, as well as the peculiarities of its spatiotemporal changes under other pathogenic (e.g., osteoporosis and osteonecrosis) conditions. In particular, higher resolution 3D mapping of bone distortions along the proximal surface and in depth seems to be extremely important for this purpose.

Supplementary Materials: The following supporting information can be downloaded at: https://www.mdpi.com/article/10.3390/cryst13030381/s1, Table S1: Information about the specimens.

Author Contributions: All authors are contributed equally to the paper. All authors have read and agreed to the published version of the manuscript.

Funding: This research was funded by Russian Science Foundation grant number 23-29-00172.

Data Availability Statement: Data are available at the Research Centers of the Science Park of St. Petersburg State University.

Acknowledgments: This research was carried out with the support of the Centre for Physical Methods of Surface Investigation, Centre for Diagnostics of Functional Materials for Medicine, Pharmacology and Nanoelectronics, and Centre for X-ray Diffraction Studies at St. Petersburg State University.

Conflicts of Interest: The authors declare no conflict of interest.

References

1. Madni, A.M. Disciplinary convergence. In *Transdisciplinary Systems Engineering*; Springer International Publishing: Cham, Switzerland, 2018; pp. 41–47.
2. Wolff, J. *Das Gesetz der Transformation der Knochen*; Hirschwald: Berlin, Germany, 1892.
3. Boyde, A.; Riggs, C.M. The quantitative study of the orientation of collagen in compact bone slices. *Bone* **1990**, *11*, 35–39. [CrossRef] [PubMed]
4. Kalmey, J.K.; Lovejoy, C.O. Collagen fiber orientation in the femoral necks of apes and humans: Do their histological structures reflect differences in locomotor loading? *Bone* **2002**, *31*, 327–332. [CrossRef] [PubMed]

5. Hong, S.I.; Hasche, L.; Bowland, S. Structural Relationships Between Social Activities and Longitudinal Trajectories of Depression Among Older Adults. *Gerontologist* **2009**, *49*, 1–11. [CrossRef] [PubMed]
6. Denisov-Nikolski, Y.I.; Mironov, S.P.; Omeljanenko, N.P. *Actual Problems of Theoretical and Clinical Osteoartrology*; Novosti Printing House: Moscow, Russia, 2005; p. 336.
7. Weiner, S.; Wagner, H.D. The Material Bone: Structure-Mechanical Function Relations. *Annu. Rev. Mater. Sci.* **1998**, *28*, 271–298. [CrossRef]
8. Currey, J.D. *Bones: Structure and Mechanics*; Princeton University Press: Princeton, NJ, USA, 2002.
9. Hancox, M.N. *Biology of Bone*; Cambridge University Press: Cambridge, UK, 1972.
10. Neuman, W.F.; Neuman, M.W. *The Chemical Dynamics of Bone Mineral*; University of Chicago Press: Chicago, CA, USA, 1958.
11. Pasteris, J.D.; Yoder, C.H.; Wopenka, B. Molecular water in nominally unhydrated carbonated hydroxylapatite: The key to a better understanding of bone mineral. *Am. Mineral.* **2014**, *99*, 16–27. [CrossRef]
12. Wilson, E.E.; Awonusi, A.; Morris, M.D.; Kohn, D.H.; Tecklenburg, M.M.J.; Beck, L.W. Three structural roles for water in bone observed by solid-state NMR. *Biophys. J.* **2006**, *90*, 3722–3731. [CrossRef]
13. Von Euw, S.; Wang, Y.; Laurent, G.; Drouet, C.; Babonneau, F.; Nassif, N. Bone mineral: New insights into its chemical composition. *Sci. Rep.* **2019**, *9*, 8456. [CrossRef]
14. Wang, Y.; Von Euw, S.; Fernandes, F.M.; Cassaignon, S.; Selmane, M.; Laurent, G.; Pehau-Arnaudet, G.; Coelho, C.; Bonhomme-Coury, L.; Giraud-Guille, M.M.; et al. Water-mediated structuring of bone apatite. *Nat. Mater.* **2013**, *12*, 1144–1153. [CrossRef]
15. Avrunin, A.S.; Denisov-Nikolsky, Y.I.; Doktorov, A.A.; Krivosenko, Y.S.; Samoilenko, D.O.; Pavlychev, A.A.; Shubniakov, I.I. The effect of water, various inclusions and substitutions on the physicochemical properties of bioapatite and the mechanical properties of mineralized tissues. *Traumatol. Ortop. Ross.* **2015**, *3*, 37–50. [CrossRef]
16. Buehler, M. Molecular nanomechanics of nascent bone: Fibrillar toughening by mineralization. *Nanotechnology* **2007**, *18*, 295102–295110. [CrossRef]
17. Avrunin, A.S.; Tihilov, R.M.; Shubniakov, I.I.; Parshin, L.A.; Melnikov, B.E.; Pliev, D.G. Hierarchy of the skeleton structure organization. Structural Relationships and Functions. *Morphology* **2010**, *6*, 69–75.
18. Fratzl, P.; Weinkamer, R. Nature's hierarchical materials. *Prog. Mater. Sci.* **2007**, *52*, 1263–1334. [CrossRef]
19. Pavlychev, A.A.; Avrunin, A.S.; Vinogradov, A.S.; Filatova, E.O.; Doctorov, A.A.; Krivosenko, Y.S.; Samoilenko, D.O.; Svirskiy, G.I.; Konashuk, A.S.; Rostov, D.A. Local electronic structure and nanolevel hierarchical organization of bone tissue: Theory and NEXAFS study. *Nanotechnology* **2016**, *27*, 504002. [CrossRef] [PubMed]
20. Hong, M.H. Biomineralization of bone tissue: Calcium-phosphate-based inorganics in collagen fibrillar organics matrices. *Biomater. Res.* **2022**, *26*, 42. [CrossRef]
21. Feng, P.; Peng, S.; Shuai, C.; Gao, C.; Yang, W.; Bin, S.; Min, A. In Situ Generation of Hydroxyapatite on Biopolymer Particles for Fabrication of Bone Scaffolds Owning Bioactivity. *ACS Appl. Mater. Interfaces* **2020**, *12*, 46743–46755. [CrossRef]
22. Sahmani, S.; Saber-Samandari, S.; Aghdam, M.M.; Khandan, A. Microstructural properties of novel nanocomposite material based on hydroxyapatite and carbon nanotubes: Fabrication and nonlinear instability simulation. *J. Nanostruct. Chem.* **2022**, *12*, 1–22. [CrossRef]
23. Dorozhkin, S.V. Calcium Orthophosphate-Containing Biocomposites and Hybrid Biomaterials for Biomedical Applications. *J. Funct. Biomater.* **2015**, *6*, 708–832. [CrossRef]
24. Sahmani, S.; Khandan, A.; Saber-Samandari, S.; Esmaeili, S.; Aghdam, M.M. Fabrication and resonance simulation of 3D-printed biocomposite mesoporous implants with different periodic cellular topologies. *Bioprinting* **2021**, *22*, e00138. [CrossRef]
25. Brykalova, X.O.; Kornilov, N.N.; Rykov, Y.A.; Cherny, A.A.; Pavlychev, A.A. Site-Dependent Peculiarities of Calcium Bonds in Bone Tissue. *J. Phys. Chem. Lett.* **2020**, *11*, 7839–7842. [CrossRef]
26. Brykalova, X.O.; Kornilov, N.N.; Cherny, A.A.; Rykov, Y.A.; Pavlychev, A.A. Elecrtronic and atomic structure of subchondral femoral bone in intact and osteoarthritic knee compartments. *Eur. Phys. J. D* **2019**, *73*, 113. [CrossRef]
27. Brykalova, X.O.; Kornilov, N.N.; Pavlychev, A.A. The peculiarities of charge distribution and spatiotemporal changes in electronic and atomic structure of bone tissue. *J. Mater. Chem. A* **2022**, *10*, 22686–22693. [CrossRef]
28. Wang, C.; Eisa, M.; Jin, W.; Shen, H.; Mi, Y.; Gao, J.; Zhou, Y.; Yao, H.; Zhao, Y. Age-related elemental change in bone. *Nucl. Instrum. Methods Phys. Res. B* **2008**, *266*, 1619–1622. [CrossRef]
29. Bonetto, L.M.; Corso PF, C.L.; Kuchar, G.G.; Gerber, J.T.; Cunha, L.F.; Elsalanty, M.; Zielak, J.C.; Gonzaga, C.C.; Scariot, R. Effect of Age and Sodium Alendronat on Femoral Fracture Repair: Biochemical and Biomechanical Study of Rats. *Front. Cell Dev. Biol.* **2021**, *9*, 558285. [CrossRef] [PubMed]
30. Thomson, J.B.; Kindt, J.H.; Drake, B.; Hansma, H.G.; Morse, D.E.; Hansma, P.K. Bone indentation recover time correlates with bond reforming time. *Nature* **2001**, *414*, 773–776. [CrossRef]
31. Currey, J.D. Sacrificial bonds heal bone. *Nature* **2001**, *414*, 699. [CrossRef]
32. Konashuk, A.S.; Samoilenko, D.O.; Klyushin, A.Y.; Svirskiy, G.I.; Sakhonenko, S.S.; Brykalova, X.O.; Kuz'mina, M.A.; Filatova, E.O.; Viogradov, A.S.; Pavlychev, A.A. Thermal changes in young and mature bone nanostructure probed with Ca 2p excitations. *Biomed. Phys. Eng. Express* **2018**, *4*, 035031. [CrossRef]
33. Nikolaev, A.; Kuz'mina, M.; Frank-Kamenetskaya, O.; Zorina, M. Influence of carbonate ion in the crystallization medium on the formation and chemical composition of CaHA–SrHA solid solutions. *J. Mol. Struct.* **2015**, *1089*, 73–80. [CrossRef]

34. Bish, D.L.; Post, J.E. Quantitative mineralogical analysis using the Rietveld full-pattern fitting method. *Am. Mineral.* **1993**, *78*, 932–940.
35. Baer, D.R.; Artyushkova, K.; Richard Brundle, C.; Castle, J.E.; Engelhard, M.H.; Gaskell, K.J.; Grant, J.T.; Haasch, R.T.; Linford, M.R.; Powell, C.J.; et al. Practical guides for x-ray photoelectron spectroscopy: First steps in planning, conducting, and reporting XPS measurements. *J. Vac. Sci. Technol. A Vac. Surf. Film. 2019 37*, 031401. [CrossRef]
36. Nesbitt, H.W.; Bancroft, G.M.; Pratt, A.R.; Scaini, M.J. Sulfur and iron surface states on fractured pyrite surfaces. *Am. Mineral.* **1998**, *83*, 1067–1076. [CrossRef]
37. Frank-Kamenetskaya, O.V.; Kol'tsov, A.B.; Kuz'mina, M.A.; Zorina, M.L.; Poritskaya, L.G. Ion substitutions and non-stoichiometry of carbonated apatite-CaOH synthesized by precipitation and hydrothermal methods. *J. Mol. Struct.* **2011**, *992*, 9–18. [CrossRef]
38. Nelson, D.G.A.; Featherstone, J.D.B. Preparation, analysis and characterization of carbonated-apatites. *Calcif. Tissue Int.* **1982**, *34*, 69–81.
39. Vignoles, M.; Bonel, G.; Holcomb, D.W.; Young, R.A. Influence of preparation conditions on the composition of type B carbonated hydroxyapatite and on the localization of the carbonate ions. *Calcif. Tissue Int.* **1988**, *43*, 33–40. [CrossRef] [PubMed]
40. Chusei, C.C.; Goodman, D.W.; Van Stipdonck, M.J.; Justes, D.R.; Schweikert, E.A. Calcium phosphate phase identification using XPS and time-of -flight cluster SIMS. *Anal. Chem.* **1999**, *71*, 149–153. [CrossRef] [PubMed]
41. Eighmy, T.T.; Kinner, A.E.; Shaw, E.L.; Euksden, J.D.; Francis, C.A. Hydroxyapatite ($Ca_5(PO_4)_3OH$) characterization by XPS: An environmentally important secondary mineral. *Surf. Sci. Spectra* **1999**, *6*, 193–201. [CrossRef]
42. Termine, J.D.; Posner, A.S. Amorphous/crystalline inter-relationships in bone mineral. *Calcif. Tissue Res.* **1967**, *1*, 8–23. [CrossRef] [PubMed]
43. Termine, J.D.; Posner, A.S. Infrared analysis of rat bone: Age dependency of amorphous and crystalline mineral fractions. *Science* **1966**, *153*, 1523–1525. [CrossRef]
44. Termine, J.D. Amorphous Calcium Phosphate: The Second Mineral of Bone. Ph.D. Thesis, Cornell University, Ithaca, NY, USA, 1966.
45. Ni, M.; Ratner, B.D. Differentiation of calcium carbonate polymorphs by surface analysis techniques–An XPS and TOF-SIMS study. *Surf. Interface Anal.* **2008**, *40*, 1356–1361. [CrossRef]
46. Feynman, R.P. Forces in molecules. *Phys. Rev.* **1939**, *56*, 340–343. [CrossRef]